ACS NANO
Cite This: ACS Nano 2019, 13, 5385−5396
www.acsnano.org

ARTICLE

Graphene Aerogel Based Bolometer for Ultrasensitive Sensing from Ultraviolet to Far-Infrared

Yangsu Xie,[†,#] Meng Han,[‡,#] Ridong Wang,[‡] Hamidreza Zobeiri,[‡] Xin Deng,[†] Peixin Zhang,[†] and Xinwei Wang*[,‡]

[†]College of Chemistry and Environmental Engineering, Shenzhen University, Shenzhen, Guangdong 518055, People's Republic of China

[‡]Department of Mechanical Engineering, Iowa State University, 2025 Black Engineering Building, Ames, Iowa 50011, United States

ABSTRACT: This work uncovers that free-standing partly reduced graphene aerogel (PRGA) films in vacuum exhibit extraordinarily bolometric responses. This high performance is mainly attributed to four structure characteristics: extremely low thermal conductivity (6.0−0.6 mW·m^{-1}·K^{-1} from 295 to 10 K), high porosity, ultralow density (4 mg·cm^{-3}), and abundant functional groups (resulting in tunable band gap). Under infrared radiation (peaked at 5.8−9.7 μm), the PRGA film can detect a temperature change of 0.2, 1.0, and 3.0 K of a target at 3, 25, and 54 cm distance. Even through a quartz window (transmissivity of ∼0.98 in the range of 2−4 μm), it can still successfully detect a temperature change of 0.6 and 5.8 K of a target at 3 and 28 cm distance. At room temperature, a laser power as low as 7.5 μW from a 405 nm laser and 5.9 μW from a 1550 nm laser can be detected. The detecting sensitivity to the 1550 nm laser is further increased by 3-fold when the sensor temperature was reduced from 295 K to 12 K. PRGA films are demonstrated to be a promising ultrasensitive bolometric detector, especially at low temperatures.

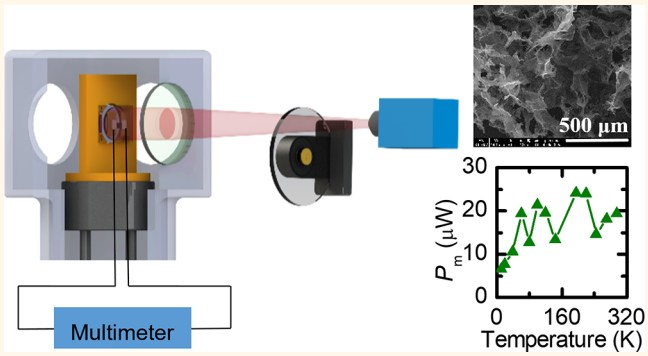

KEYWORDS: *graphene aerogels, bolometers, ultraviolet, far-infrared, ultrasensitive sensing*

Bolometers have booming applications in both civilian and military fields including thermal imaging, night vision, astronomy, security, building heat leaks tracking, and particle physics. Various materials such as amorphous Si (a-Si), alloys and oxides of Si and Ge, and oxides of transition metals[1−3] have been reportedly used as detectors for infrared (IR), visible, and ultraviolet (UV) light in major commercially available products. Recently, Au-decorated ZnO microwires were reported for detecting and processing optical stimuli into electronic controlling signals in piezo-phototronic logic computations.[4] a-Si and vanadium oxide are the most common sensing materials. a-Si can easily be integrated into complementary metal oxide semiconductor (CMOS) fabrication, is highly stable, and has a fast time constant and a long mean time before failure.[5] Vanadium oxide is well studied for fabrication of an uncooled bolometer due to its phase transition behavior at around the 67−68 °C range.[6−8] In spite of successful commercialization of the above bolometric materials, detectors that combine wideband and ultrasensitive performance, affordability, and convenience of operation are still in great demand.

Traditional bolometers consist of two essential elements: absorber and sensor. Thermal radiation is absorbed by the absorber, leading to a temperature rise. It subsequently results in a change in electrical resistance in the sensor, which can be measured using electric circuits. The thermal response of bolometers can be simplified as $C\,dT/dt = P(t) - G(T - T_s)$, where C is the heat capacitance, P is the radiation power, G is the thermal conductance, and T_s is the surrounding temperature. This equation shows that to achieve a high sensitivity, the bolometer system requires the following key properties: very high IR absorption,[9] a high temperature coefficient of the resistance (φ), and as small as possible G. Furthermore, to have a fast time response, the bolometer's heat capacitance (C) needs to be as small as possible. However, a small C always leads to a very small size of bolometer, which will increase G significantly. Therefore, in practice, a bolometer has to be thermally weakly connected to the circuit to decrease G.

Received: January 2, 2019
Accepted: April 18, 2019
Published: April 18, 2019

DOI: 10.1021/acsnano.9b00031
ACS Nano 2019, 13, 5385−5396

Although a high sensitivity has been achieved by complex designs, more accessible materials with self-absorption and self-sensing (better affordability and convenience of operation) should be invented to speed up the pace of bolometer application.

The optical properties of graphene suggest outstanding potential for applications in nanoscale-sized optoelectronics.[10−12] Graphene has wideband photon absorption from ultraviolet to a few 100 μm due to the interband transitions.[13−15] The absorption coefficient of the incident light for a single-layered graphene is 2.3%,[15,16] which is remarkably high for an atomically thin material. The small Fermi surface makes the electron−phonon interaction in graphene very weak even at room temperature. As a result, graphene-based bolometers should have very small electron−phonon thermal conductivity and high intrinsic sensitivity as a photodetector.[17−19] However, due to the weak electron−phonon interaction, the electrical resistance of graphene is only weakly dependent on temperature, which makes simple resistive readout difficult. To achieve a high φ value, an energy gap needs to be introduced. Several methods have been reported, including applying a strong magnetic field to form Landau levels,[18] inducing a band gap in bilayer graphene,[20] using superconducting tunnel junctions,[21] introducing structural defects,[22,23] or oxygen-containing functional groups.[22,24,25]

Graphene aerogel (GA) is an interconnected, porous 3D framework constructed with randomly assembled reduced graphene oxide (rGO) sheets. GA has a very high specific surface area, good compressibility, and ultralow density and is electrically conductive, which makes it promising for wide applications including composites,[26] sensors,[27] environmental treatment,[28] energy storage such as microsupercapacitors,[29] *etc.* Inherited from the excellent photon absorption properties of graphene and graphene oxide (GO),[30] GA is expected to present a high and wideband photon absorption. Its highly porous and rough surface also plays an important role in enhancing the photon absorption through an internal trapping effect. Self-assembling of rGO flakes induced by chemical reduction is one of the most common methods for synthesizing GA. A chemical reduction process introduces functional groups (such as N- and S-containing functional groups) as well as leaving residual oxygen-containing functional groups onto graphene flakes. As a result, GA is expected to present a very high φ. In addition, the thermal conductivity (k) of ultralight GA is extremely low. Our past work reported that the k of GA ($(4.7−5.9) \times 10^{-3}$ W m^{-1} K^{-1}) at room temperature (RT) is about 80% lower than that of still air (0.0257 W m^{-1} K^{-1} at 20 °C).[31] The ultralow k is important for reducing thermal dissipation, which is promising for improving the sensitivity of the bolometer. Furthermore, the lowest density reported for GA reached as low as 0.16 mg·cm^{-3}.[32] The ultralow density results in very small volumetric heat capacitance (ρc_p) of GA, which is desirable for fast heating and response to incident radiation. By using GA as both absorber and sensor, the dilemma of achieving as small as possible G and low C is expected to be solved. Therefore, chemically reduced GA with various functional groups is a very appealing candidate for bolometric applications. However, a GA-based bolometer has not been studied so far.

In this work, we prepare partly reduced GA (PRGA) synthesized by a chemical reduction method and explore its limit of detection sensitivity as a bolometer. The high φ and ultralow k, which are key properties for the bolometric performance, are presented and discussed. The bolometric response of free-standing PRGA films for a wide spectrum from ultraviolet to far-infrared, with varying optical power and over the temperature range of 12−295 K, are studied. The origin of photoresponse is investigated and demonstrated to be bolometric.

RESULTS AND DISCUSSION

Structure of PRGA. The as-prepared PRGA film is shown in Figure 1(a). The film can be cut into a rectangular shape.

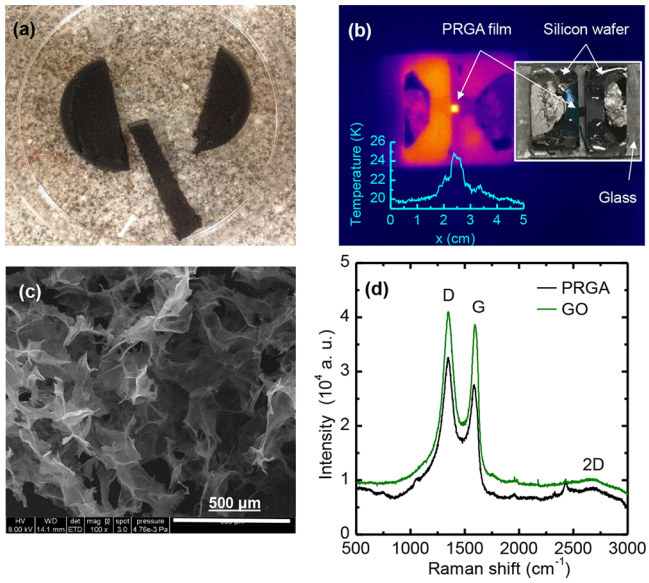

Figure 1. (a) Digital camera image of PRGA film. (b) Infrared image of a suspended PRGA sample under uniform laser irradiation. The upper inset shows a photograph; the lower inset presents the temperature distribution along the horizontal direction. (c) Porous structure under SEM. (d) Raman spectrum of PRGA and GO.

During the photoresponse test, the films are clamped tightly between two layers of silicon wafers by using metal clips (removed later) and epoxy resin and then suspended on a glass substrate. The inset in Figure 1(b) shows a photograph of a suspended PRGA sample. Figure 1(b) presents an infrared image under uniform laser irradiation. The temperature distribution along the horizontal direction is also presented. It can be seen that the temperature of the PRGA sample is much higher than the electrode areas. Under the scanning electron microscope (SEM), a three-dimensional porous structure with pore sizes ranging from tens to hundreds of micrometers can be observed [Figure 1(c)]. The effect of increased hydrophobicity and $\pi-\pi$ interactions during chemical reduction results in randomly assembled partly reduced graphene oxide (prGO) sheets. The Raman spectrum of the PRGA film shows two pronounced peaks, the D mode (1348 cm^{-1}) and G mode (1585 cm^{-1}) [Figure 1(d)]. The G mode is originated from stretching of the C−C bond in graphitic materials, which is usually assigned to zone center phonons of E_{2g} symmetry.[33] The D peak at around 1348.1 cm^{-1} is due to the breathing mode of sp^2 atoms in rings, which reflects the structural disorder.[34] For comparison, the bands at around 1350 and 1610 cm^{-1} corresponding to the D and G modes of GO are also presented in the figure. The intensity of

DOI: 10.1021/acsnano.9b00031
ACS Nano 2019, 13, 5385−5396

the D peak to that of the G peak (I_D/I_G) of PRGA is 1.13, higher than that of GO (1.06). The fwhm of PRGA is further determined to be 59.0 cm^{-1}, which is lower than that of GO (66.2 cm^{-1}). The combined result of I_D/I_G and fwhm uncovers a decreased defect density resulting from chemical reduction. The fwhm of the G peak always increases with disorder.[35,36] The increased I_D/I_G has been commonly reported for chemically reduced graphene oxide. Since GO and PRGA have a high number of defects, the sp^2 clusters are small (clusters size L_D < 3 nm) and distorted. Under this situation, the development of the D peak actually indicates ordering, which is opposite that of graphene.[33,36] During the chemical reduction process, the precursor GO has been partly reduced by ethylenediamine (EDA) and the defect density is decreased.

The X-ray diffraction (XRD) patterns of PRGA film [Figure 2(a)] show three major peaks located at around 17.59°, 21.35°, and 26.38°, respectively. The interlayer spacing is calculated to be 3.395−5.065 Å according to Bragg's law. For comparison, the precursor GO shows an interlayer spacing of 7.46 Å from its 11.9° 2θ peak, which is also presented in Figure 2(a). The interlayer spacing of graphite was reported to be 3.36 Å from graphite's (002) plane.[37] The result indicates that there are functional groups remaining in the interlayer of PRGA. Figure 2(b) shows the Fourier-transform infrared spectroscopy (FTIR) spectra, which qualitatively reveals the functional groups responsible for the absorption from 600 to 3600 cm^{-1}. The band at 1080 cm^{-1} corresponds to the epoxy groups. The bands at 1425, 1599, and 3423 cm^{-1} can be assigned to $-CH_2$, N−H, and −OH groups, respectively.[38−40] This indicates that some incident light can be resonantly absorbed by the various functional groups on PRGA films. The presence of epoxy groups indicates mild reduction of GO in PRGA. With further reduction, the peak corresponding to epoxy groups is expected to disappear.[39] The elemental composition and functional groups are characterized by X-ray photoelectron spectroscopy (XPS). Figure 2(c) shows the XPS survey of PRGA and its precursor GO. The total atomic concentration of the PRGA film surface is 83.3% C, 7.0% N, and 9.7% O. In comparison, the total atomic concentration of GO is 65.5% C and 34.5% O. Figure 2(d) shows the deconvoluted C 1s spectrum of PRGA and GO, respectively. The fitting of the C 1s spectrum further confirms the presence of epoxy groups and hydroxyl groups in PRGA. The deconvoluted N 1s spectrum of PRGA in Figure 2(e) indicates the existence of several N-containing functional groups including pyridinic N (398.6 eV), pyrrolic N (400.6 eV), and oxidized N groups (403.8 eV).[41]

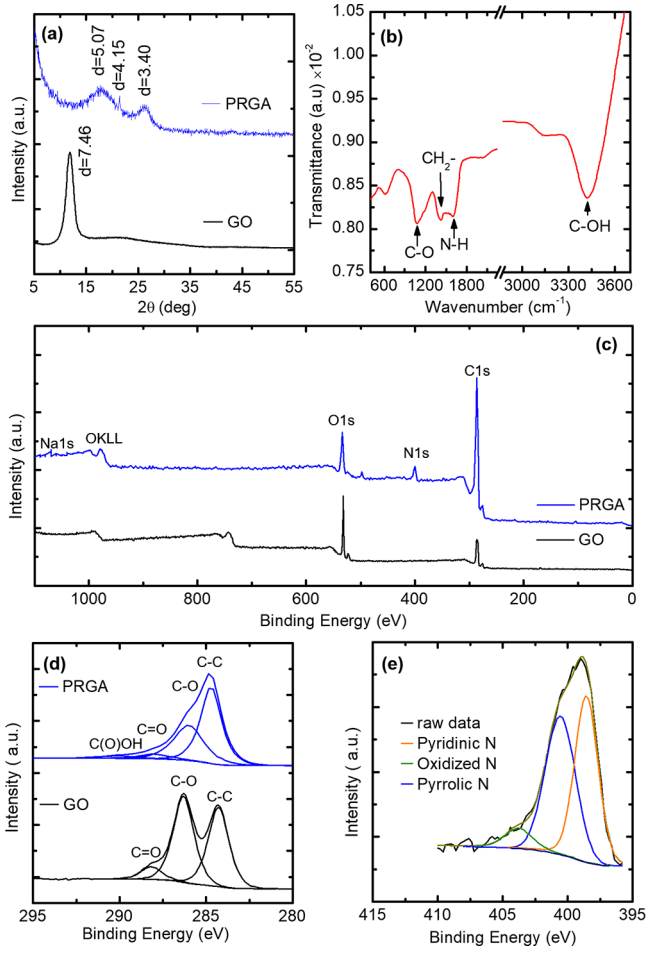

Figure 2. Structural characterization of PRGA. (a) XRD spectrum of PRGA and GO. (b) FTIR spectrum of PRGA. (c) XPS spectrum survey of PRGA and GO. (d) Deconvoluted C 1s spectrum of PRGA and GO. (e) Deconvoluted N 1s spectrum of PRGA.

Significantly Improved Temperature Sensitivity. The temperature coefficient of resistance (φ) is a key property to evaluate the bolometric performance, as the responsivity is proportional to the slope of the electrical resistance *versus* temperature ($R-T$) curve: dR/dT. The most common material for the thermistor part of microbolometers is vanadium oxide (VO_x) due to its high φ value. At the transition temperature (67−68 °C), the electrical resistivity undergoes a drastic change (on the order of 10^5) over a temperature interval of 0.1 K.[42] The measured φ of vanadium oxide (VOx) thin film[43,44] were reported to be −2.6% to −2.8% K^{-1} at RT. However, high-temperature annealing (~500 °C) after deposition is necessary, which would increase the fabrication costs. In addition, reproducibility of properties suffers in the higher φ-value films, and heating becomes a problem with high resistivity films.

The schematic of the experimental setup for measuring φ of PRGA film is shown in Figure 3(a). Figure 4(a) shows the temperature-dependent R of three PRGA film. The three samples are denoted as s1, s2, and s3, the dimensions of which can be found in Table 1. R of PRGA films shows semiconductive $R-T$ behaviors with a fast increase at low temperatures. As temperature goes down from 295 K to 10 K, R increases by up to 8.2 times. Figure 4(b) shows the relative φ [$\varphi\% = dR/(dT\ R_T)$] as a function of environmental temperature T, where R_T is the resistance at temperature T. At 295 K, φ is about 0.3% K^{-1} (3.83−5.96 $\Omega\cdot K^{-1}$). As the temperature goes down to 10 K, φ reaches 2.9% K^{-1} (298.50 $\Omega\cdot K^{-1}$) at 10 K. Compared to graphene, φ of PRGA film (0.3% K^{-1} at RT) is much higher. φ of graphene was reported to be 0.02−0.05% K^{-1} at 260−350 K.[45]

The $R-T$ curve sheds light on the electron transport mechanisms in PRGA. R of PRGA is related to many factors. It has been reported that the $R-T$ curve in carbon materials was a combined effect of thermal activation, the nearest-neighbor hopping (NNH),[46] and variable range hopping (VRH). In different temperature regimes, different mechanisms could dominate.[47] In the thermal activation process, the electrons are thermally excited from the Fermi level to the conduction bands. In the NNH process, the electrons are excited from the

DOI: 10.1021/acsnano.9b00031
ACS Nano 2019, 13, 5385−5396

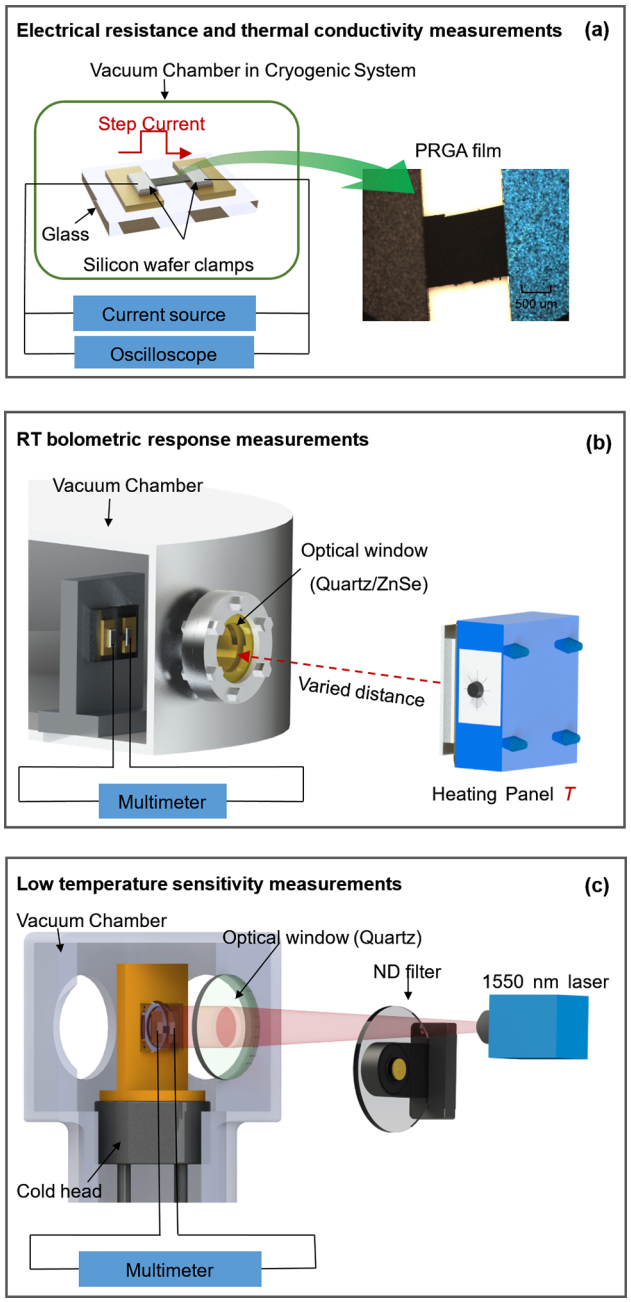

Figure 3. Schematic of the experimental setup for measuring (a) the electrical resistance and thermal conductivity, (b) the bolometric response at room temperature, and (c) the bolometric sensitivity to a 1550 nm laser at low temperature and the origin of the photoresponse.

occupied levels to nearest-neighbor unoccupied levels. If thermal activation or NNH dominates, the logarithmic R is expected to be linearly dependent on T^{-1}.[47,48] The VRH model assumes that the transport of electrons occurs *via* hopping to other conducting areas with the same energy levels at remote locations. The $R-T$ behavior of the VRH model in a two-dimensional system can be derived as $R = R_0 \exp(T_0/T^{1/3})$, in which R_0 is the initial resistance and T_0 is the characteristic temperature,[45] which can be calculated as $T_0 = [3/(N(\varepsilon_F)k_B l_L^2)]^{1/3}$, where $N(\varepsilon_F)$ is the density of states at the Fermi level, k_B the Boltzmann constant, and l_L the

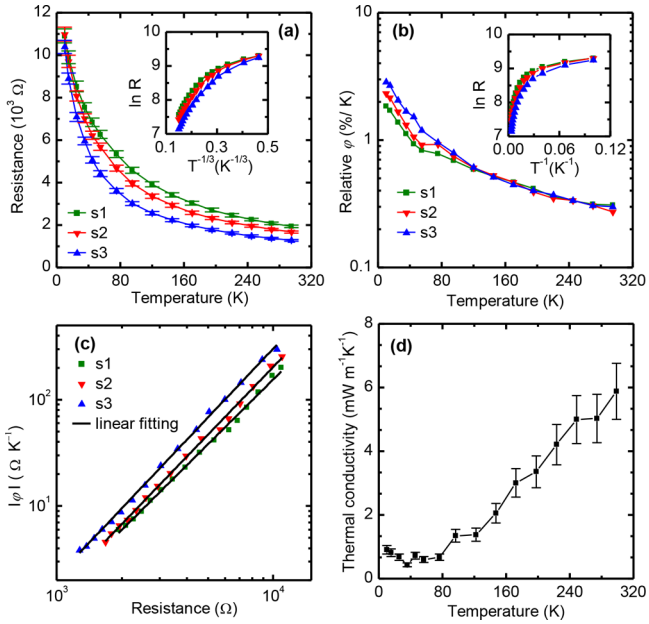

Figure 4. Electrical transport properties of PRGA. (a) Electrical resistivity between 10 and 295 K. The inset shows the $\ln(R)-T^{-1/3}$ curve. (b) Relative φ against temperature between 10 and 295 K. The inset shows the $\ln(R)-T^{-1}$ curve. (c) φ *versus* low-bias resistance. (d) Thermal conductivity of the PRGA film against temperature.

Table 1. Details of the PRGA Film Samples in This Work

sample index	s1	s2	s3	s4	s5	s6	s7
suspended length [mm]	4.9	3.4	2.6	3.2	2.2	1.4	1.2
width [mm]	1.7	1.7	1.7	4.9	4.9	1.2	1.0
thickness [mm]	1.0	1.0	1.0	1.1	1.1	0.3	0.2

localized length.[48] Thus, if VRH dominates, the logarithmic R is expected to linearly dependent on $T^{-1/3}$.

Kaiser *et al.* found that the electrical conduction in rGO can be explained by the VRH model.[49] Eda *et al.* also reported that the mechanism of electron transport in lightly reduced GO is VRH, whereas thermal activation begins to dominate in well-reduced GO.[48] The VRH conduction was found to dominate in fluorinated[50] and hydrogenated graphene.[51] Bae *et al.* reported the electrical transport properties of both mildly reduced GO and strongly reduced GO between 260 and 350 K can be fitted well using the two-dimensional VRH model.[45] Han *et al.* also found a linear dependence in the logarithmic resistance against the $T^{-1/3}$ curve of the disordered graphene in the temperature range of 1.5 to 300 K.[23] However, as shown in the inset of Figure 4(a) and (b), neither the $\ln(R)-T^{-1/3}$ nor the $\ln(R)-T^{-1}$ curves of PRGA films are linear. This indicates that the electron transport in the PRGA film in the temperature range of 295−10 K cannot be fully characterized by the two-dimensional electron transport model. Sun *et al.* also found a nonlinear $\ln(R)-T^{-1}$ behavior for single polycrystalline−amorphous carbon nanocoils over a temperature range of 4 to 300 K. To fit the data, different mathematic models including thermal activation, NNH, Mott VRH, and Efrose−Shklovskiiare VRH are used to separately fit the $\ln(R)$ data in five different temperature regimes, respectively.[47]

As shown in Figure 4(c), φ of the PRGA films is strongly correlated with R. A linear correlation between the logarithmic φ and logarithmic R, $[\lg(\varphi) \sim \lg(R)]$, is found. The linear

DOI: 10.1021/acsnano.9b00031
ACS Nano 2019, 13, 5385−5396

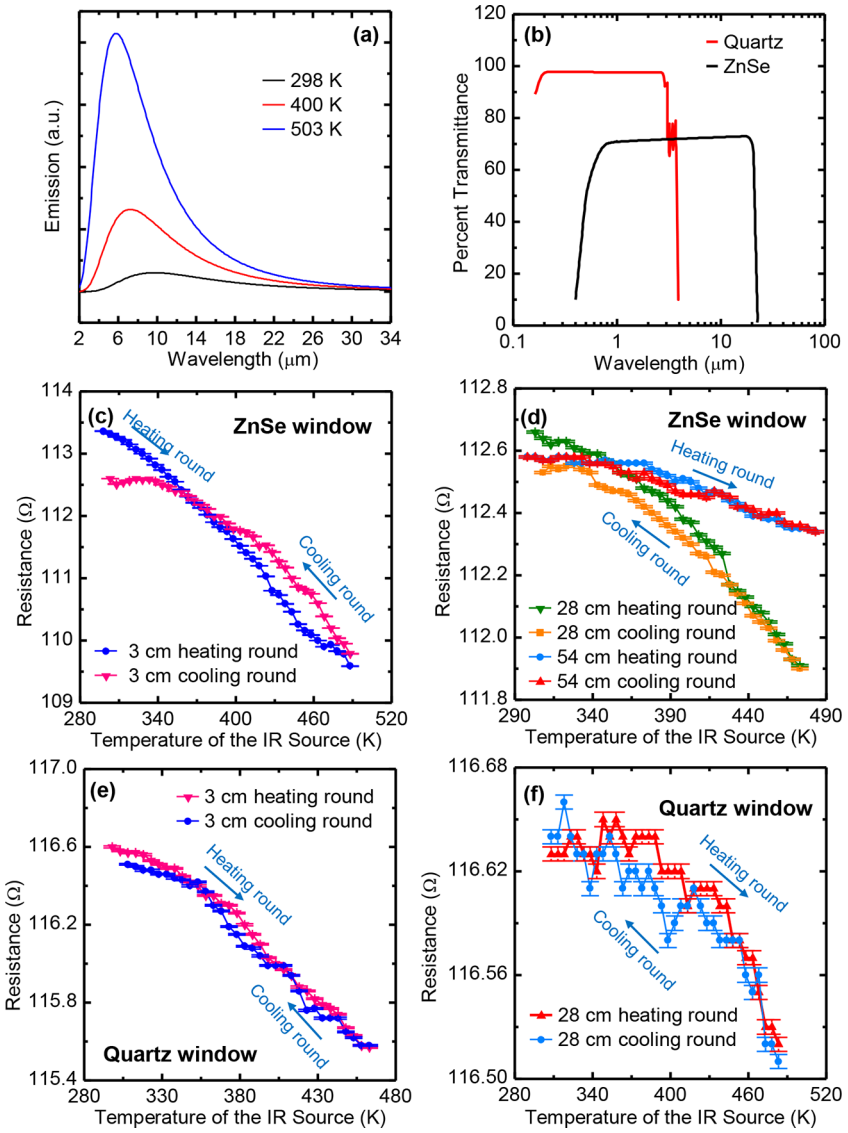

Figure 5. (a) Wavelength-dependent radiation power distribution of the blackbody radiation at a temperature of 298, 400, and 503 K. (b) Transmission spectrum for ZnSe and quartz windows. The electrical resistance of the sample *versus* the surface temperature of the IR source (c, d) through the ZnSe window and (e, f) through a quartz window.

relationship was also reported by Dickerson *et al.* in bulk 4 μm thick, free-standing rGO ribbons, while the reason has not been elucidated.[22] We linearly fitted the $\lg(\varphi)-\lg(R)$ curves of PRGA films. A correlation between R and φ, $\log(-\varphi) = aR^n + b$, is obtained, where a, b, and n are constants determined from the $\lg(\varphi)-\lg(R)$ curve. For our three PRGA samples, n is determined to be 2.03−2.15. It should be noted that this correlation applies to the electrically conductive behavior of the three PRGA films in the temperature range of RT to 10 K. By using this single $\varphi-R$ model, the temperature-dependent behavior of R of PRGA can be characterized with great accuracy.

We attribute this $R-T$ correlation and high φ to the combined effect of electrons hopping and temperature-dependent electrical contact resistance among neighboring prGO flakes within the bulk PRGA material. As shown in the XPS and FTIR results, a large amount of residual oxygen and nitrogen-containing functional groups are decorated on the prGO flakes in PRGA. Previous work suggested the presence of an energy gap in GO the size of which was dependent on the fraction of sp^2/sp^3-hybridized domains.[52,53] Vlassiouk *et al.* found the electrical resistivity of graphene produced by the CVD method showed a linear correlation with L_a^{-1}, where L_a is the characteristic domain size.[54] Thus, the functional groups as well as other structural defects in PRGA lead to a band gap and impart insulating behavior. As demonstrated above, VRH is expected to dominate in individual prGO flakes.[45,49] Electrons hop between localized states corresponding to the sp^2 grains which have a lower energy difference. In addition, the electrons captured in the states induced by functional groups or defects are expected to be more easily excited to CB owing to the low-energy difference between CB and VB. Furthermore, since the PRGA film is a bulk nanostructured material, the interfaces among neighboring prGO flakes also play an important role in the $R-T$ behavior. The contact among the prGO flakes becomes worse due to the temperature decrease, which inevitably increases the electrical contact resistance. R of the PRGA film is influenced by the combined effect of VRH and temperature-dependent electrical contact resistance. As a result, it increases exponentially with reduced temperature at

DOI: 10.1021/acsnano.9b00031
ACS Nano 2019, 13, 5385−5396

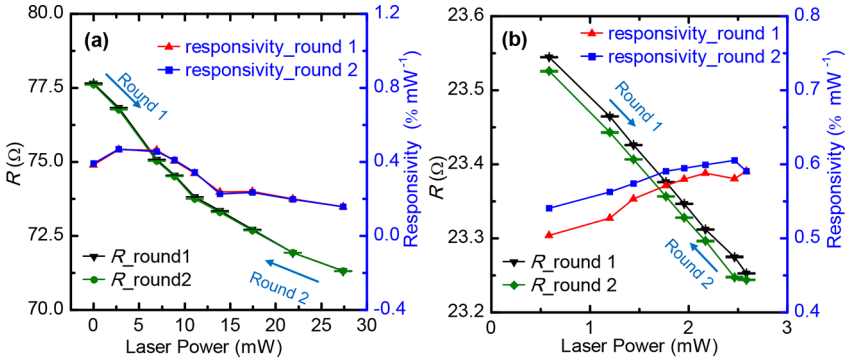

Figure 6. Resistance and resistive responsivity in percentage over the original resistance *versus* the incident laser power of (a) the 405 nm wavelength laser and (b) the 1550 nm wavelength laser.

low temperatures. This could also be applied to explain the reported $R-T$ behavior of bulk free-standing rGO ribbons.[22]

Substantially Reduced Thermal Conductance. As shown in Figure 4(d), the measured k in vacuum is about 6.0 mW·m^{-1}·K^{-1} at 295 K, which is much lower than that of air (25.7 mW·m^{-1}·K^{-1} at RT). As the temperature goes down, k even decreases to as low as ∼0.6 mW·m^{-1}·K^{-1} in the temperature range of 10−80 K. It is widely accepted that phonons are the main heat carriers in graphene. Large amount of residual oxygen-containing functional groups exist, and abundant nitrogen-containing functional groups are decorated onto prGO flakes in PRGA, which provide numerous scattering sites for phonons. The existence of other defects including single vacancy, double vacancy, and Stone−Wales defects can also significantly reduce the thermal conductivity by increasing the phonon scattering intensity. In addition, the interflakes' connection within PRGA is mainly *via* van der Waals force and $\pi-\pi$ stacking, which leads to significant interface thermal contact resistance. Thus, the ultralow k of PRGA can be ascribed to the extremely low density, structural defect-induced phonon scattering, as well as significant thermal contact resistance among neighboring prGO sheets.[31]

The extremely low k of the PRGA films is another important property that makes it a promising candidate for highly sensitive bolometric detecting material. As introduced in the introduction section, the thermal response of a bolometer can be described by $CdT/dt = P(t) - G(T - T_s)$. Thus, reducing the material's thermal link (G) to the environment is indispensable in order to obtain an adequate bolometric photoresponse. To achieve this, some previous work designed a thermal barrier between graphene and electrical contacts such as a boron nitride (BN) layer.[23] For the PRGA films, its k is extremely low due to its structure characteristics. Thus, the use of extra thermal barriers can be avoided since the heat dissipation through diffusion is already substantially reduced in PRGA. Under the same IR illumination, the temperature increase of PRGA films can be much higher than that of 2D graphene/rGO. In addition, the high porosity ($\varphi \approx 99.8\%$) endows PRGA films with an ultralow density ($\rho \approx 4$ mg·cm^{-3}), which makes the volumetric heat capacity (ρc_p) sufficiently small. The extremely low k and low ρc_p contribute to a high responsivity of the PRGA-based bolometer.

Broadband Bolometric Response at RT. The resistive bolometric response in the mid-infrared and far-infrared range is measured by irradiating the PRGA film sample (s4, details in Table 1) with IR radiation from a heating plate, which emits a broad spectrum. The experimental setup is shown in Figure 3(b). Figure 5(a) shows the wavelength-dependent radiation power distribution of the blackbody radiation at a temperature of 298, 400, and 503 K (typical temperatures of the heating plate). The radiation wavelength ranges from 2 μm (5000 cm^{-1}) to 34 μm (294 cm^{-1}) with a peak at 5.8−9.7 μm according to the Wien displacement law. The heating plate is made of a white enameled stainless steel panel with an emissivity of about 0.85−0.91.[55,56] The transmission range is 0.6−20 μm for ZnSe [Figure 5(b)] with a transmissivity of ∼0.71.[57] Figure 5(c) and (d) show R of the sample *versus* T_s of the IR source through a ZnSe window. Most of the incident IR from the IR source can pass through the ZnSe window to irradiate the sample. When the IR source is placed at a distance of 3 cm from the PRGA sample, R shows a strong correlation with T_s. R decreases from 113.36 Ω to 109.59 Ω as T_s increases from 298 K to 488 K. When the IR source is placed at a distance of 28 cm, the resistance decreases from 112.66 Ω to 111.90 Ω as T_s increases from 298 K to 473 K. Even when the IR source is moved 54 cm away, R still shows a strong correlation and decreases from 112.58 Ω to 112.34 Ω as T_s increases from 298 K to 483 K. The resolution of the 8 $^1/_2$ digit digital multimeter used in this work is 10 μΩ when the to-be-measured resistance range is 1.0 kΩ. The disturbance from the resistance variation due to the unstable electrical contact resistance within the PRGA film as well as that between the PRGA film and the silicon electrodes (noises) is determined by the standard deviation of the resistance, which is measured 14 times, and the value is calculated to be 0.004 Ω. (details can also be found in the Methods section). This indicates that the stability of resistance of s4 is about 0.004 Ω. Therefore, when the IR source is at a distance of 3 cm, the minimum T_s variation of the IR source that our PRGA bolometer can detect is 0.2 K. When the IR source is placed 28 and 54 cm away, the minimum detectable T_s variation is 1.0 and 3.0 K, respectively.

Figure 5(e) and (f) show the R of the sample *versus* T_s of the IR source through the quartz window. The IR grade fused quartz has a transmission range of 2 μm to around 4 μm [Figure 5(b)] with a transmissivity of ∼0.98. The heating plate as an IR source gives IR light of wavelength ranging from 2 μm (5000 cm^{-1}) to 34 μm (294 cm^{-1}) with a peak at 5.8−9.7 μm. Through the fused quartz window, only a small part of the incident radiation (wavelength between 2 and 4 μm) can pass through the fused quartz window. Nevertheless, R is still sensitive to T_s. When the IR source is placed at 3 cm distance, R of s4 decreases from 116.58 Ω to 115.58 Ω as T_s is increased from 298 K to about 463 K. When the IR source is moved to 28 cm away from PRGA sample, R shows a decreasing

DOI: 10.1021/acsnano.9b00031
ACS Nano 2019, 13, 5385−5396

behavior from 116.64 Ω to 116.52 Ω as T_s is increased from 308 K to 483 K. Taking the resistance stability of s4 into consideration, the minimum detectable T_s change is about 0.6 K at 3 cm distance. Although R becomes less sensitive to the changing T_s of the IR source at a 28 cm distance, the $R-T_s$ correlation is still strong when T_s is higher than 393 K. This indicates that the PRGA film can successfully detect a temperature variation of 5.8 K of an IR source through a quartz window at 28 cm distance when the target temperature is higher than 393 K. It can be seen from Figure 5(a), when T_s of the IR source is lower than 393 K, most of the irritated IR radiation is out of the transmission range of the quartz window. It can be seen that the $R-T_s$ curve of the heating round agrees well with that of the cooling round, which demonstrates that the bolometric response of the PRGA film sample has good repeatability.

To study the bolometric response to photons of shorter wavelengths, two lasers of wavelengths of 405 and 1550 nm are selected to test the resistive responsivity of the PRGA film to the variation of the incident laser power (P) illuminating the PRGA sample. Two samples are measured (s5 for the 405 nm laser and s6 for the 1550 nm laser, details in Table 1). The quartz window is used, and it has a high transmissivity at 405 and 1550 nm (~0.934 for 405 nm and ~0.946 for 1550 nm). The $R-P$ curve is measured twice, which is denoted as round 1 and round 2. The left y axis in Figure 6(a) and (b) shows the $R-P$ curve for the 405 and 1550 nm lasers, respectively. For both lasers, R decreases as P is increased. It can be seen that the data of the two rounds of experiments are consistent, which demonstrates a good repeatability. For the 1550 nm laser, when the laser power is 2.58 mW (1.54 mW·mm^{-2}), the resistance change of s6 between laser-off and laser-on is 0.36 Ω, which is a 1.52% change over the original resistance. The obtained characteristics are compared with the commercial[44,58,59] and other bolometric materials presented by Yan *et al.*,[20] Zhang *et al.*,[60] and Itkis *et al.*[61] and are summarized in Table 2. It can be seen from the table that the φ of PRGA at 10 K is comparable to that of vanadium oxide and a-Si, which have very high resistivity. The PRGA film shows a higher φ and sensitivity than the reported MWCNT films, SWCNT films, and dual-gated bilayer graphene.

Table 2. Comparison of the Bolometric Effect-Based Photodetector Performance

material type	absolute φ	$\Delta R/R$ or $\Delta V/V$ and incident IR/laser intensity	response time	ref
a-Si	2.5%/K at RT			62
a-Si:H,B	2.8%	10^6 V/W	11 ms	58
a-SiGe:H,F	3.7% at RT	1.9 × 10^6 V/W at I = 550 nA	300−500 ms	59
vanadium oxide film	2.6−2.8%/K at 300 K	2.12%/W		43, 44
MWNT films	0.07%/K	1.2% at 3.5 mW/mm^2[a]	1−2.5 ms	63
SWNT films	0.17%/K	0.3% at 3.5 mW/mm^2[a]	40−50 ms	64
dual-gated bilayer graphene		1.88% at 8 mW/mm^2 at 5 K[a]	0.25 ns at 4.55 K and 0.1 ns at 10 K	20
PRGA film	0.3%/K at 295 K, 2.9%/K at 10 K	1.52% at 1.54 mW/mm^2 (1550 nm laser)	0.4 ms (0.2 mm long)	this work

[a]Calculated from the reference data.

The resistive responsivity is further investigated. $|dR/dP|$ is determined by measuring the resistance change dR between the laser-on and laser-off conditions. The resistive responsivity in percentage over the original resistance ($|dR/dP|/R$) is calculated and plotted against P in the right y axis in Figure 6(a) and (b). For the 405 nm laser, the incident laser power is varied from 0 to 27.4 mW, and the corresponding responsivity is in the range of 0.16%·mW^{-1} (0.11 Ω·mW^{-1}) to 0.47%·mW^{-1} (0.36 Ω·mW^{-1}) with a peak at 2.77 mW. For the 1550 nm laser, the responsivity varied from 0.50%·mW^{-1} (0.12 Ω·mW^{-1}) to 0.61%·mW^{-1} (0.14 Ω·mW^{-1}) when the laser power is varied from 0.59 mW to 2.58 mW. The responsivities of the 405 and 1550 nm lasers are comparable. After taking the resistance stability (2.7 × 10^{-3} Ω for s5 and 8.3 × 10^{-4} Ω for s6) into consideration, a laser power as low as 7.5 μW from the 405 nm laser and a laser power as low as 5.9 μW from the 1550 nm laser can be detected by the PRGA bolometer.

Bolometric Response at Low Temperatures with Significant Improvement in Sensitivity. For PRGA films, φ increases sharply [Figure 4(a) and (b)] and k decreases [Figure 4(d)] at low temperatures. As a result, the responsivity of PRGA films is expected to be significantly improved if the environmental temperature T is lowered. Therefore, we further explore the limit of bolometric detectivity of PRGA films to the 1550 nm laser at low temperatures. The experimental setup is shown in Figure 3(c). The resistance variation due to laser power change (dR/dP) of s7 (details in Table 1) is measured and presented in Figure 7(a). At 295 K, dR/dP is about −52.05 Ω·W^{-1}. As the temperature decreases to 12 K, dR/dP increases by almost 7-fold, reaching −391.85 Ω·W^{-1}. The original resistance at 295 K is 28.366 Ω. Thus, the resistive

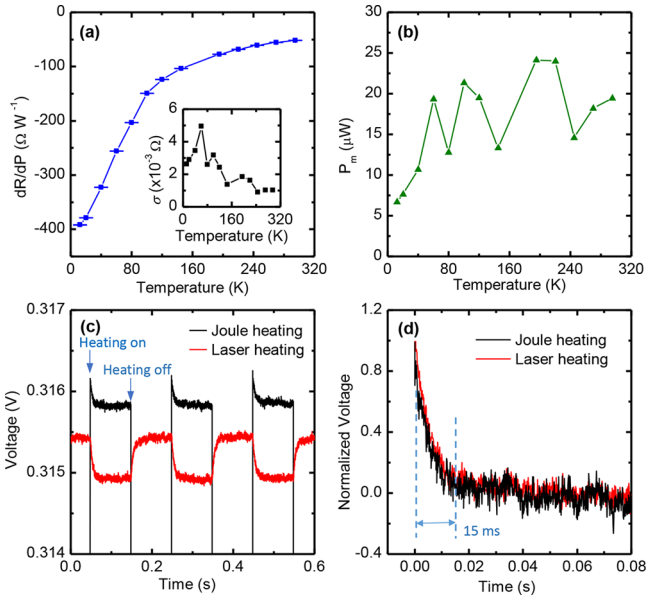

Figure 7. (a) Resistive responsivity to 1550 nm laser irradiation in the temperature range of 12−295 K. The inset shows the standard deviation of the resistance. (b) Minimum detectable laser power of 1550 nm wavelength in the temperature range of 12−295 K. (c) Voltage−time profiles under laser heating and joule heating (with offset for comparison). (d) Comparison of normalized voltage *versus* time profiles between laser heating and joule heating, which confirms that the response times are consistent and the photoresponse to the laser is a heating effect.

DOI: 10.1021/acsnano.9b00031
ACS Nano 2019, 13, 5385−5396

responsivity in percentage is 0.18%·mW^{-1} at 295 K and reaches as high as 1.38%·mW^{-1} at 12 K.

To show the minimum laser energy that this PRGA bolometer can detect, the disturbance from the resistance variation (noises) should be taken into consideration. At each temperature, the resistances in the laser-off and laser-on conditions (R_{off} and R_{on}) are measured more than 14 times, and the standard deviation of the resistance (σ) is calculated. The inset in Figure 7(a) shows σ of R_{off} obtained at different temperatures. σ ranges from 8.89×10^{-4} to 4.95×10^{-3} Ω. The small variation of the resistance results from the electrical contact resistance between the PRGA film and the electrodes.

The minimum laser power variation that the PRGA bolometer can detect is determined by $P_m = \sigma\, dP/dR$. As shown in Figure 7(b), at 12 K, P_m reaches 6.7 μW. At 295 K, P_m is about 19.5 μW. This indicates that our PRGA bolometer can detect laser energy as low as 19.5 μW at 295 K and 6.7 μW at 12 K. In the experimental setup, no structure optimization, light focusing, or signal amplification equipment have been used. The PRGA film is simply clamped by using silicon wafers and epoxy resin adhesives. In the future, by using sophisticated methods to connect the PRGA film with the electrodes, the electrical contact resistance is expected to be significantly reduced. The multimeter has a high resolution of 1×10^{-5} Ω when the resistance range is 1.0 KΩ. If the σ of resistance is reduced to the order of 10^{-5} Ω with sound electrode connection, the whole system can be further optimized, which can improve the detectivity of the PRGA-based bolometer significantly.

Physics of Photoresponse and the Response Time. The key principle of photodetection is the conversion of absorbed photons into electrical signals. Since the whole PRGA film is under a uniform and constant IR/laser illumination during the measurements, the temperature distribution along the length direction is symmetric around the middle point. Therefore, photothermoelectric signals cannot be generated. Photovoltaic current generation is based on the separation of photogenerated electron−hole (e−h) pairs by built-in electric fields. In the case of graphene, a photovoltaic effect produced by the external electric field is generally avoided since graphene is a semimetal and therefore it generates a large dark current.[65] Considering the possibilities that the origin of photoresponse in PRGA can be either photovoltaic or bolometric, the voltage transient behavior induced by laser irradiation is compared with that induced by joule heating. The photoswitching behavior of the PRGA bolometer (s7) under the 5 Hz square-wave-modulated laser illumination is presented in Figure 7(c) with offset. Upon laser illumination, the voltage of the sample decreases and reaches a steady state. In the comparative experiment, a square-wave current of 10 mA in amplitude and 5 Hz in frequency is applied to induce a joule heating to compare with the response to the modulated laser. Upon joule heating, the temperature of the sample increases and then reaches a steady state. The corresponding voltage profile is also presented in Figure 7(c). We found excellent agreement of the normalized voltage−time profiles (V^*-t) between the two responses to the laser illumination and joule heating [Figure 7(d)]. It can be seen clearly that the two response curves show the same decay times (~15 ms). This justifies that the origin of the photoresponse of the PRGA is bolometric.

Therefore, the working micromechanism of the PRGA film can be described as follows. Under IR/laser irradiation, the energy of the incident IR/laser radiation results in photoexcited carriers (excitons).[61] Electron−phonon interactions lead to ultrafast relaxation of the photoexcited carriers, and the energy is efficiently transferred to the crystal lattice. Subsequently, the temperature rise of the crystal lattice contributes to the electrical resistance change in two mechanisms. On one hand, it could provide more scattering opportunities for the electrons, which increase the electrical resistance. On the other hand, more electrons could be thermally excited from the valence band into the conduction band by the temperature increase, which decreases the electrical resistance. In PRGA films, the second mechanism dominates. Thus, the electrical resistance of PRGA films presents a decreasing behavior under the incident IR/laser radiation.

From the V^*-t curve, the response time of the PRGA films is identified when V^* is decreased by 0.95. For s7 with a suspended length of 1.2 mm, the response time is about 15 ms, corresponding to a framing rate of 67 per second. Previous work reported that the response time for a photothermal effect based carbon nanotube photodetector was about 1−50 ms.[60,61,63] Itkis *et al.* found the response time for 3.5 mm long suspended single-walled carbon nanotube films was 50 ms.[61] Assuming a one-dimensional heat transfer model for the photothermal effect based sample, the characteristic time (Δt_c), which is defined from the normalized temperature *versus* time curve when the normalized temperature rise reaches 0.8665, can be determined as $\Delta t_c = 0.2026L^2/\alpha$, where L is the suspended length and α is thermal diffusivity of the suspended sample.[66,67] It can be seen from this equation that the bolometric response time for a suspended material is dependent on L^2 as well as α of the material. The ultralow α and k of PRGA are desirable for improving the responsivity since dT can be significantly increased, while the response time is slightly compromised. However, considering the suspended sample length in our work is quite long (1.2 mm), if the suspended length of the sample is reduced to 0.2 mm, the response time of the PRGA bolometer can be significantly reduced to 1/36 of the original response time, which becomes 0.4 ms. This corresponds to a framing rate of 2500 per second. The response time of the PRGA film is compared with that of commercial and other bolometric materials (Table 2). The PRGA film shows a faster response than the reported MWCNT films, SWCNT films, and a-Si. Combined with the high φ, low k, and high sensitivity, PRGA films may become competitive for practical application of IR detection with further optimization.

CONCLUSION

In summary, chemically reduced PRGA films by using EDA as reduction agent show excellent bolometric performance. With the high density of nitrogen and oxygen-containing functional groups, ultralow density (~ 4 mg·cm^{-3}), and self-assembled 3D structure, the PRGA films are endowed with high φ, low C, and extremely low k. The resistive response to photons with different wavelengths, varying power, and under different environmental temperature (295−12 K) was characterized to uncover the ultrahigh sensitivity of the PRGA-based bolometer. When a target (radiation: 2 to 34 μm peaked at 5.8−9.7 μm) was at a distance of 3, 28, and 54 cm, the minimum detectable surface temperature variation is 0.2, 1.0, and 3.0 K, respectively. Even through a quartz window that only allows very weak IR (2−4 μm) radiation to pass, the

DOI: 10.1021/acsnano.9b00031
ACS Nano 2019, 13, 5385−5396

PRGA film can still successfully detect a temperature variation of 0.6 and 5.8 K for a target at 3 and 28 cm distance. At RT, a laser power as low as 7.5 μW from a 405 nm laser and a laser power as low as 5.9 μW from a 1550 nm laser can be detected by the PRGA bolometer. The detecting sensitivity to a 1550 nm laser is further increased by 3-fold when the sensor temperature was lowered from 295 K to 12 K. The response time for a 1.2 mm long sample was determined to be ~15 ms. The change in electrical resistance during the photon detection was discovered to be bolometric (heating by incident photons) instead of photovoltaic. The bolometric response of free-standing PRGA films is demonstrated to be very promising such that they may function as the ultrasensitive element of an IR bolometric detector, especially at low temperatures.

METHODS

Materials. PRGA is synthesized by mild chemical reduction of GO using EDA as the reduction agent, followed by freeze-drying and subsequent microwave reduction.[39] A GO dispersion in water (concentration of 5 g·L^{-1} and C/O ratio of about 4) was purchased from Graphene Supermarket Company. EDA anhydrous (99.9%) was obtained from Fisher Scientific and used as received. Briefly, EDA (4 μL) is diluted with deionized water (2 mL) and then mixed with a GO (3 mL) dispersion under magnetic stirring. The mixture is then poured into a quartz mold and heated in an oven at 95 °C for 6 h to obtain a graphene hydrogel film. After that, the hydrogel is subjected to freeze-drying to completely remove the solvent. Then the sample is placed at the bottom of a long quartz tube and flushed with argon gas for 2 h to remove air. After that, the tube is sealed and a fast microwave heating (15 s) is applied to the sample to restore the $\pi-\pi$ interaction in the cross-linking sites and to enhance the elastic stiffness.[39] The free-standing PRGA films (around 3 cm in diameter and 4 mg·cm^{-3} in density) are then obtained.

Structure Characterization. In order to study the structural properties of samples, we used SEM, XRD, Raman spectroscopy, FTIR, and XPS (Figures 1 and 2). The SEM images are taken by using an FEI Quanta 250 field emission SEM with a voltage of 8.00 kV. Raman spectra are obtained by using Olympus BX51 (532 nm laser excitation). The X-ray diffraction is conducted with a Siemens D500 X-ray diffractometer using a Cu X-ray tube operated at 45 kV and 30 mA. Chemical analysis of PRGA is conducted by XPS on a PHI55000 XPS with an Al Kα source (1486.6 eV). The FTIR spectra are obtained using a PerkinElmer FTIR spectrometer. The sample for FTIR characterization is obtained by mixing a small amount of PRGA with KBr and then compressing the mixture into tablets.

Temperature Coefficient of Resistance Measurement. Before measuring φ, the PRGA films are cut into rectangular shape. The films are clamped tightly between two layers of silicon wafers by using metal clips and epoxy resin and then suspended on a glass substrate [Figure 1(b)]. The whole sample is mounted on the stage of a cold head in a closed-cycle cryostat system (Janis, CCS), which is utilized to control and monitor the environmental temperature. A small amount of silver paste is applied to connect the electrodes to wirings. The whole stage is then shielded with a radiation shield and sealed in a vacuum chamber. During the measurement, R is measured by using a current source (Keithley) and an oscilloscope (Tektronix MDO) in 2-point configurations, with a small bias current (I) applied and voltage (V) probed. R is then calculated by $R = V/I$ and obtained from 295 K down to 10 K.

Thermal Conductance Characterization. Thermophysical properties of carbon nanostructures have been widely studied by using various methods, including the electrical self-heating method,[68] Raman optothermal method,[69−71] and theoretical simulations.[72] In this work, k of PRGA is measured using the steady-state electro-thermal (SET) technique from 295 to 10 K. The experimental configuration is shown in Figure 3(a). The suspended sample is then put on the cold head of the CCS system. The vacuum chamber is pumped to an air pressure lower than 0.5 mTorr to reduce the effect of heat convection to a negligible level. A small step current is applied to the sample to induce a joule heating. Assuming a one-dimensional heat conduction model, when the temperature of the sample becomes stable at the current-on stage, the governing equation for energy balance can be expressed as $k_m\partial^2T(x)/\partial x^2 + q_0 = 0$, in which k_m is the effective thermal conductivity, which includes the radiation effect. $T(x)$ is the temperature at the x position, and $q_0 = I^2R_1/A_cL$ is the joule heating rate per unit volume. I is the current applied to the sample, R_1 is the resistance at the steady state during current-on, and A_c and L are the cross-section area and length of the sample, respectively. Solving the governing equation, k_m is then determined by

$$k_m = \frac{I^2R_1L}{12A_c\Delta R}\frac{dR}{dT} \quad (1)$$

In this equation, ΔR is the resistance change induced by the joule heating. dR/dT is obtained by differentiating the $R-T$ curve. Three PRGA film samples s1, s2, and s3 have the same width and thickness (D), while the suspended lengths (L) are different (Table 1). During the measurement, the thermal radiation effect is related to L as $k_m = k + 8\varepsilon_r\sigma T^3L^2/(D\pi^2)$,[73,74] in which $\varepsilon_r \approx 1$ is the emissivity of PRGA, $\sigma = 5.67 \times 10^{-8}$ W·m^{-2}·K^{-4} is the Stefan−Boltzmann constant, and T is the environmental temperature. Thus, the real thermal conductivity (k) is then obtained by linearly extrapolating the k_m-L^2 curve to the point of $L^2 = 0$. The k measurement is conducted every 5−25 K from 295 to 10 K. More details about the SET technique can be found in our past work.[75,76]

Bolometric Response Measurement. The resistive bolometric response in the mid-infrared and far-infrared range at RT is measured by illuminating the PRGA films with IR radiation from a heating plate (Corning hot plate Scholar 170, with a 5 × 5 in. white enameled stainless steel panel). The surface temperature of the panel (T_s) is adjusted from 298 to 503 K, which is recorded by a thermocouple attached to the panel surface. Two kinds of optical windows including quartz (diameter 37 mm) and zinc selenide (ZnSe, diameter 22 mm) are used to provide a different transmission range. Furthermore, to test the bolometric response of PRGA films in the visible−near-infrared range, two lasers with wavelengths of 405 nm (diode laser, 80 mW) and 1550 nm (diode laser, 5W) are used as light sources. The laser power is adjusted and measured, which provides different incident optical power. As shown in Figure 3(b), s4 is suspended between two gold-coated silicon electrodes and connected to a multimeter (Keithley 2002 8 $^1/_2$ digit digital multimeter). Then the whole stage is vertically mounted on an aluminum block and placed near the optical window (distance ~3 cm) in a vacuum chamber. The incident IR/lasers are aligned along the center line of the PRGA films. During the measurement, the IR/laser spot covers the whole PRGA film. The distance between the surface of the heating plate and the PRGA sample is varied from 3 to 54 cm. The air pressure in the vacuum chamber is maintained below 30 mTorr. The two-point R of the PRGA film is measured and recorded simultaneously by using the multimeter. To verify the repeatability and correlation of the bolometric response, T_s of the heating plate is decreased back and R is recorded again. The two rounds of experiments are denoted as the heating round and the cooling round, respectively.

To measure the bolometric response and detectivity to the 1550 nm laser at low temperatures (12−295 K), the sample (s7, Table 1) is suspended using the same method as that described above. The experimental setup is shown in Figure 3(c). The optical window of the cryogenic system is made of quartz and has a diameter of 41 mm. During the measurement, the laser spot fully covers the whole sample. The temperature of the cold head is controlled and monitored from 295 to 12 K. The air pressure in the chamber is maintained below 0.5 mTorr. The detectivity is determined by measuring R_{off} and R_{on} using the 8 $^1/_2$ digit digital multimeter. The change of resistance from laser-off condition to laser-on condition is calculated as $dR = R_{off} - R_{on}$. The laser power illuminating the surface of the sample through the cryogenic optical window is measured to be $dP = 2$ mW.

Physics of Photoresponse and the Response Time Measurement. The sample (s7) is suspended as described above. For the laser

DOI: 10.1021/acsnano.9b00031
ACS Nano 2019, 13, 5385−5396

heating experiment, the 1550 nm laser is used as the light source. The output of the laser is modulated to be a 5 Hz square wave by using a function generator (Stanford Research Systems, model DS345). The two electrodes of the sample are connected to a current source and an oscilloscope. By applying a small DC current to the sample, at which no appreciable heating occurs, the two-point voltage profiles under the square-wave laser illumination are recorded by the oscilloscope. In the comparative experiment, a square-wave current of 10 mA in amplitude and 5 Hz in frequency is applied to induce a joule heating to check its response and to compare with the response to the modulated laser.

AUTHOR INFORMATION

Corresponding Author

*E-mail (X. Wang): xwang3@iastate.edu.

ORCID

Xinwei Wang: 0000-0002-9373-3750

Author Contributions

#Y. Xie and M. Han contributed equally to this work.

Notes

The authors declare no competing financial interest.

ACKNOWLEDGMENTS

Support of this work by the Start-up Fund of Shenzhen University (85303-00000138) and Scientific Research Foundation for Talented Scholars in Shenzhen (827-000360) is gratefully acknowledged.

REFERENCES

(1) Soref, R. Mid-Infrared Photonics in Silicon and Germanium. *Nat. Photonics* **2010**, *4*, 495−497.

(2) Rogalski, A. Recent Progress in Infrared Detector Technologies. *Infrared Phys. Technol.* **2011**, *54*, 136−154.

(3) Michel, J.; Liu, J. F.; Kimerling, L. C. High-Performance Ge-on-Si Photodetectors. *Nat. Photonics* **2010**, *4*, 527−534.

(4) Li, H. X.; Liu, N. S.; Zhang, X. H.; Su, J.; Li, L. Y.; Gao, Y. H.; Wang, Z. L. Piezotronic and Piezo-Phototronic Logic Computations Using Au Decorated Zno Microwires. *Nano Energy* **2016**, *27*, 587−594.

(5) Weiler, D.; Hochschulz, F.; Busch, C.; Stein, M.; Michel, M. D.; Würfel, D.; Lerch, R.; Petermann, M.; Geruschke, T.; Blaeser, S.; Weyers, S.; Vogt, H. Uncooled digital IRFPA-family with 17μm pixel-pitch based on amorphous silicon with massively parallel Sigma-Delta-ADC readout. In *Infrared Technology and Applications XLIV*, Proc. SPIE, Orlando, FL, USA, 2018; Vol. *10624*, p 1062419.

(6) Sumesh, M. A.; Karanth, S.; Prakash, S.; Laxmiprasad, A. S.; Nagendra, C. L. Ion Beam Sputtered Ge-Si-O Amorphous Thin Films for Microbolometer Infrared Detectors and Their Application in Earth Sensors. *Sens. Actuators, A* **2013**, *192*, 81−91.

(7) Marchese, L. E.; Thomas, P.; Pope, T. D.; Asselin, D.; Jerominek, H. A Compact Lightweight Earth Horizon Sensor Using an Uncooled Infrared Bolometer. *Proc. SPIE* **2007**, *6796*, 679629.

(8) Sumesh, M. A.; Thomas, B.; Vijesh, T. V.; Rao, G. M.; Viswanathan, M.; Karanth, S. P. Optically Immersed Bolometer Ir Detectors Based on V2O5 Thin Films with Polyimide Thermal Impedance Control Layer for Space Applications. *J. Infrared, Millimeter, Terahertz Waves* **2018**, *39*, 6−23.

(9) Chattopadhyay, S.; Huang, Y. F.; Jen, Y. J.; Ganguly, A.; Chen, K. H.; Chen, L. C. Anti-Reflecting and Photonic Nanostructures. *Mater. Sci. Eng., R* **2010**, *69*, 1−35.

(10) Vasko, F. T.; Ryzhii, V. Photoconductivity of Intrinsic Graphene. *Phys. Rev. B: Condens. Matter Mater. Phys.* **2008**, *77*, 195433.

(11) Xia, F. N.; Mueller, T.; Lin, Y. M.; Valdes-Garcia, A.; Avouris, P. Ultrafast Graphene Photodetector. *Nat. Nanotechnol.* **2009**, *4*, 839−843.

(12) Mueller, T.; Xia, F. N. A.; Avouris, P. Graphene Photodetectors for High-Speed Optical Communications. *Nat. Photonics* **2010**, *4*, 297−301.

(13) Dawlaty, J. M.; Shivaraman, S.; Strait, J.; George, P.; Chandrashekhar, M.; Rana, F.; Spencer, M. G.; Veksler, D.; Chen, Y. Q. Measurement of the Optical Absorption Spectra of Epitaxial Graphene from Terahertz to Visible. *Appl. Phys. Lett.* **2008**, *93*, 131905−0.

(14) Li, Z. Q.; Henriksen, E. A.; Jiang, Z.; Hao, Z.; Martin, M. C.; Kim, P.; Stormer, H. L.; Basov, D. N. Dirac Charge Dynamics in Graphene by Infrared Spectroscopy. *Nat. Phys.* **2008**, *4*, 532−535.

(15) Nair, R. R.; Blake, P.; Grigorenko, A. N.; Novoselov, K. S.; Booth, T. J.; Stauber, T.; Peres, N. M. R.; Geim, A. K. Fine Structure Constant Defines Visual Transparency of Graphene. *Science* **2008**, *320*, 1308−1308.

(16) Kuzmenko, A. B.; van Heumen, E.; Carbone, F.; van der Marel, D. Universal Optical Conductance of Graphite. *Phys. Rev. Lett.* **2008**, *100*, 117401.

(17) Du, X.; Prober, D. E.; Vora, H.; Mckitterick, C. B. Graphene-Based Bolometers. *Graphene 2D Mater.* **2014**, *1*, 1−22.

(18) Kalugin, N. G.; Jing, L.; Bao, W. Z.; Wickey, L.; Del Barga, C.; Ovezmyradov, M.; Shaner, E. A.; Lau, C. N. Graphene-Based Quantum Hall Effect Infrared Photodetector Operating at Liquid Nitrogen Temperatures. *Appl. Phys. Lett.* **2011**, *99*, No. 013504.

(19) Sun, D.; Aivazian, G.; Jones, A. M.; Ross, J. S.; Yao, W.; Cobden, D.; Xu, X. D. Ultrafast Hot-Carrier-Dominated Photocurrent in Graphene. *Nat. Nanotechnol.* **2012**, *7*, 114−118.

(20) Yan, J.; Kim, M. H.; Elle, J. A.; Sushkov, A. B.; Jenkins, G. S.; Milchberg, H. M.; Fuhrer, M. S.; Drew, H. D. Dual-Gated Bilayer Graphene Hot-Electron Bolometer. *Nat. Nanotechnol.* **2012**, *7*, 472−478.

(21) Vora, H.; Kumaravadivel, P.; Nielsen, B.; Du, X. Bolometric Response in Graphene Based Superconducting Tunnel Junctions. *Appl. Phys. Lett.* **2012**, *100*, 4855−111.

(22) Dickerson, W.; Hemsworth, N.; Gaskell, P.; Ledwosinska, E.; Szkopek, T. Bolometric Response of Free-Standing Reduced Graphene Oxide Films. *Appl. Phys. Lett.* **2015**, *107*, 1308.

(23) Han, Q.; Gao, T.; Zhang, R.; Chen, Y.; Chen, J.; Liu, G.; Zhang, Y.; Liu, Z.; Wu, X.; Yu, D. Highly Sensitive Hot Electron Bolometer Based on Disordered Graphene. *Sci. Rep.* **2013**, *3*, 3533.

(24) Evlashin, S.; Dyakonov, P.; Khmelnitsky, R.; Dagesyan, S.; Klokov, A.; Sharkov, A.; Timashev, P.; Minaeva, S.; Maslakov, K.; Svyakhovskiy, S.; Suetin, N. Controllable Laser Reduction of Graphene Oxide Films for Photoelectronic Applications. *ACS Appl. Mater. Interfaces* **2016**, *8*, 28880−28887.

(25) Liang, H. Mid-Infrared Response of Reduced Graphene Oxide and Its High-Temperature Coefficient of Resistance. *AIP Adv.* **2014**, *4*, No. 013106.

(26) Ramanathan, T.; Abdala, A. A.; Stankovich, S.; Dikin, D. A.; Herrera-Alonso, M.; Piner, R. D.; Adamson, D. H.; Schniepp, H. C.; Chen, X.; Ruoff, R. S.; Nguyen, S. T.; Aksay, I. A.; Prud'homme, R. K.; Brinson, L. C. Functionalized Graphene Sheets for Polymer Nanocomposites. *Nat. Nanotechnol.* **2008**, *3*, 327−331.

(27) Shao, Y. Y.; Wang, J.; Wu, H.; Liu, J.; Aksay, I. A.; Lin, Y. H. Graphene Based Electrochemical Sensors and Biosensors: A Review. *Electroanalysis* **2010**, *22*, 1027−1036.

(28) Sui, Z. Y.; Meng, Q. H.; Zhang, X. T.; Ma, R.; Cao, B. Green Synthesis of Carbon Nanotube-Graphene Hybrid Aerogels and Their Use as Versatile Agents for Water Purification. *J. Mater. Chem.* **2012**, *22*, 8767−8771.

(29) Yue, Y.; Liu, N.; Ma, Y. A.; Wang, S. L.; Liu, W. J.; Luo, C.; Zhang, H.; Cheng, F.; Rao, J. Y.; Hu, X. K.; Su, J.; Gao, Y. H. Highly Self-Healable 3d Microsupercapacitor with Mxene-Graphene Composite Aerogel. *ACS Nano* **2018**, *12*, 4224−4232.

(30) Li, D.; Muller, M. B.; Gilje, S.; Kaner, R. B.; Wallace, G. G. Processable Aqueous Dispersions of Graphene Nanosheets. *Nat. Nanotechnol.* **2008**, *3*, 101−105.

DOI: 10.1021/acsnano.9b00031
ACS Nano 2019, 13, 5385−5396

(31) Xie, Y. S.; Xu, S.; Xu, Z. L.; Wu, H. C.; Deng, C.; Wang, X. W. Interface-Mediated Extremely Low Thermal Conductivity of Graphene Aerogel. *Carbon* **2016**, *98*, 381−390.
(32) Sun, H. Y.; Xu, Z.; Gao, C. Multifunctional, Ultra-Flyweight, Synergistically Assembled Carbon Aerogels. *Adv. Mater.* **2013**, *25*, 2554−2560.
(33) Ferrari, A. C.; Robertson, J. Interpretation of Raman Spectra of Disordered and Amorphous Carbon. *Phys. Rev. B: Condens. Matter Mater. Phys.* **2000**, *61*, 14095−14107.
(34) Ferrari, A. C. Raman Spectroscopy of Graphene and Graphite: Disorder, Electron-Phonon Coupling, Doping and Nonadiabatic Effects. *Solid State Commun.* **2007**, *143*, 47−57.
(35) Ferrari, A. C.; Rodil, S. E.; Robertson, J. Interpretation of Infrared and Raman Spectra of Amorphous Carbon Nitrides. *Phys. Rev. B: Condens. Matter Mater. Phys.* **2003**, *67*, 155306−0.
(36) Ferrari, A. C.; Basko, D. M. Raman Spectroscopy as a Versatile Tool for Studying the Properties of Graphene. *Nat. Nanotechnol.* **2013**, *8*, 235−246.
(37) Park, S.; An, J.; Potts, J. R.; Velamakanni, A.; Murali, S.; Ruoff, R. S. Hydrazine-Reduction of Graphite- and Graphene Oxide. *Carbon* **2011**, *49*, 3019−3023.
(38) Che, J. F.; Shen, L. Y.; Xiao, Y. H. A New Approach to Fabricate Graphene Nanosheets in Organic Medium: Combination of Reduction and Dispersion. *J. Mater. Chem.* **2010**, *20*, 1722−1727.
(39) Hu, H.; Zhao, Z. B.; Wan, W. B.; Gogotsi, Y.; Qiu, J. S. Ultralight and Highly Compressible Graphene Aerogels. *Adv. Mater.* **2013**, *25*, 2219−2223.
(40) Acik, M.; Lee, G.; Mattevi, C.; Chhowalla, M.; Cho, K.; Chabal, Y. J. Unusual Infrared-Absorption Mechanism in Thermally Reduced Graphene Oxide. *Nat. Mater.* **2010**, *9*, 840−845.
(41) Mahmood, N.; Zhang, C. Z.; Yin, H.; Hou, Y. L. Graphene-Based Nanocomposites for Energy Storage and Conversion in Lithium Batteries, Supercapacitors and Fuel Cells. *J. Mater. Chem. A* **2014**, *2*, 15−32.
(42) Kim, D. H.; Kwok, H. S. Pulsed-Laser Deposition of Vo2 Thin-Films. *Appl. Phys. Lett.* **1994**, *65*, 3188−3190.
(43) Ozcelik, A.; Cabarcos, O.; Allara, D. L.; Horn, M. W. Vanadium Oxide Thin Films Alloyed with Ti, Zr, Nb, and Mo for Uncooled Infrared Imaging Applications. *J. Electron. Mater.* **2013**, *42*, 901−905.
(44) Kumar, R. T. R.; Karunagaran, B.; Mangalaraj, D.; Narayandass, S. K.; Manoravi, P.; Joseph, M.; Gopal, V.; Madaria, R. K.; Singh, J. P. Room Temperature Deposited Vanadium Oxide Thin Films for Uncooled Infrared Detectors. *Mater. Res. Bull.* **2003**, *38*, 1235−1240.
(45) Bae, J. J.; Yoon, J. H.; Jeong, S.; Moon, B. H.; Han, J. T.; Jeong, H. J.; Lee, G. W.; Hwang, H. R.; Lee, Y. H.; Jeong, S. Y.; Lim, S. C. Sensitive Photo-Thermal Response of Graphene Oxide for Mid-Infrared Detection. *Nanoscale* **2015**, *7*, 15695−15700.
(46) Choi, T. Y.; Poulikakos, D.; Tharian, J.; Sennhauser, U. Measurement of Thermal Conductivity of Individual Multiwalled Carbon Nanotubes by the 3-Ω Method. *Appl. Phys. Lett.* **2005**, *87*, No. 013108.
(47) Sun, Y. M.; Wang, C. W.; Pan, L. J.; Fu, X.; Yin, P. H.; Zou, H. L. Electrical Conductivity of Single Polycrystalline-Amorphous Carbon Nanocoils. *Carbon* **2016**, *98*, 285−290.
(48) Eda, G.; Mattevi, C.; Yamaguchi, H.; Kim, H.; Chhowalla, M. Insulator to Semimetal Transition in Graphene Oxide. *J. Phys. Chem. C* **2009**, *113*, 15768−15771.
(49) Kaiser, A. B.; Gomez-Navarro, C.; Sundaram, R. S.; Burghard, M.; Kern, K. Electrical Conduction Mechanism in Chemically Derived Graphene Monolayers. *Nano Lett.* **2009**, *9*, 1787−1792.
(50) Hong, X.; Cheng, S. H.; Herding, C.; Zhu, J. Colossal Negative Magnetoresistance in Dilute Fluorinated Graphene. *Phys. Rev. B: Condens. Matter Mater. Phys.* **2011**, *83*, 1041−1043.
(51) Elias, D. C.; Nair, R. R.; Mohiuddin, T. M. G.; Morozov, S. V.; Blake, P.; Halsall, M. P.; Ferrari, A. C.; Boukhvalov, D. W.; Katsnelson, M. I.; Geim, A. K.; Novoselov, K. S. Control of Graphene's Properties by Reversible Hydrogenation: Evidence for Graphane. *Science* **2009**, *323*, 610−613.
(52) Jeong, H. K.; Jin, M. H.; So, K. P.; Lim, S. C.; Lee, Y. H. Tailoring the Characteristics of Graphite Oxides by Different Oxidation Times. *J. Phys. D: Appl. Phys.* **2009**, *42*, No. 065418.
(53) Mathkar, A.; Tozier, D.; Cox, P.; Ong, P. J.; Galande, C.; Balakrishnan, K.; Reddy, A. L. M.; Ajayan, P. M. Controlled, Stepwise Reduction and Band Gap Manipulation of Graphene Oxide. *J. Phys. Chem. Lett.* **2012**, *3*, 986−991.
(54) Vlassiouk, I.; Smirnov, S.; Ivanov, I.; Fulvio, P. F.; Dai, S.; Meyer, H.; Chi, M. F.; Hensley, D.; Datskos, P.; Lavrik, N. V. Electrical and Thermal Conductivity of Low Temperature Cvd Graphene: The Effect of Disorder. *Nanotechnology* **2011**, *22*, 275716.
(55) Optotherm Support: Emissivity in the Infrared. https://www.optotherm.com/emiss-table.htm (accessed October 9, 2018).
(56) Technical Information: Radiation Infrared Heating- Theory& Principle. https://www.infraredheaters.com/pdfs/radiant.pdf (accessed October 9, 2018).
(57) Thorlabs: Zinc Selenide (Znse) Windows. https://www.thorlabschina.cn/NewGroupPage9.cfm?objectgroup_id=3981 (accessed September 10, 2018).
(58) Syllaios, A. J.; Schimert, T. R.; Gooch, R. W. Amorphous Silicon Microbolometer Technology. *MRS Online Proc. Libr.* **2000**, *609*, DOI: 10.1557/PROC-609-A14.4.
(59) Garcia, M.; Ambrosio, R.; Torres, A.; Kosarev, A. Ir Bolometers Based on Amorphous Silicon Germanium Alloys. *J. Non-Cryst. Solids* **2004**, *338*, 744−748.
(60) Zhang, S.; Cai, L.; Wang, T.; Miao, J.; Sepulveda, N.; Wang, C. Fully Printed Flexible Carbon Nanotube Photodetectors. *Appl. Phys. Lett.* **2017**, *110*, 123105.
(61) Itkis, M. E.; Borondics, F.; Yu, A. P.; Haddon, R. C. Bolometric Infrared Photoresponse of Suspended Single-Walled Carbon Nanotube Films. *Science* **2006**, *312*, 413−416.
(62) Razeghi, M. *Handbook of Infrared Detection Technologies*; Elsevier, 2002.
(63) Lu, R. T.; Shi, J. J.; Baca, F. J.; Wu, J. Z. High Performance Multiwall Carbon Nanotube Bolometers. *J. Appl. Phys.* **2010**, *108*, 1857.
(64) Lu, R. T.; Li, Z. Z.; Xu, G. W.; Wu, J. Z. Suspending Single-Wall Carbon Nanotube Thin Film Infrared Bolometers on Microchannels. *Appl. Phys. Lett.* **2009**, *94*, 163110.
(65) Koppens, F. H. L.; Mueller, T.; Avouris, P.; Ferrari, A. C.; Vitiello, M. S.; Polini, M. Photodetectors Based on Graphene, Other Two-Dimensional Materials and Hybrid Systems. *Nat. Nanotechnol.* **2014**, *9*, 780−793.
(66) Guo, J. Q.; Wang, X. W.; Wang, T. Thermal Characterization of Microscale Conductive and Nonconductive Wires Using Transient Electrothermal Technique. *J. Appl. Phys.* **2007**, *101*, 2996−125.
(67) Parker, W. J.; Jenkins, R. J.; Abbott, G. L.; Butler, C. P. Flash Method of Determining Thermal Diffusivity, Heat Capacity, and Thermal Conductivity. *J. Appl. Phys.* **1961**, *32*, 1679−0.
(68) Li, Q. Y.; Takahashi, K.; Ago, H.; Zhang, X.; Ikuta, T.; Nishiyama, T.; Kawahara, K. Temperature Dependent Thermal Conductivity of a Suspended Submicron Graphene Ribbon. *J. Appl. Phys.* **2015**, *117*, No. 065102.
(69) Liu, J. H.; Li, T. Y.; Hu, Y. D.; Zhang, X. Benchmark Study of the Length Dependent Thermal Conductivity of Individual Suspended, Pristine Swcnts. *Nanoscale* **2017**, *9*, 1496−1501.
(70) Liu, J. H.; Xie, H. H.; Hu, Y. D.; Zhang, X.; Zhang, Y. Y. Thermal Transport in Suspended Swcnts at High Heat Fluxes. *Int. J. Heat Mass Transfer* **2017**, *108*, 572−576.
(71) Li, Q. Y.; Xia, K. L.; Zhang, J.; Zhang, Y. Y.; Li, Q. Y.; Takahashi, K.; Zhang, X. Measurement of Specific Heat and Thermal Conductivity of Supported and Suspended Graphene by a Comprehensive Raman Optothermal Method. *Nanoscale* **2017**, *9*, 10784−10793.
(72) Zhang, J. C.; Wang, X. W. Thermal Transport in Bent Graphene Nanoribbons. *Nanoscale* **2013**, *5*, 734−743.
(73) Lin, H.; Xu, S.; Wang, X. W.; Mei, N. Significantly Reduced Thermal Diffusivity of Free-Standing Two-Layer Graphene in Graphene Foam. *Nanotechnology* **2013**, *24*, 415706.

DOI: 10.1021/acsnano.9b00031
ACS Nano 2019, 13, 5385−5396

(74) Xie, Y. S.; Xu, Z. L.; Xu, S.; Cheng, Z.; Hashemi, N.; Deng, C.; Wang, X. W. The Defect Level and Ideal Thermal Conductivity of Graphene Uncovered by Residual Thermal Reffusivity at the 0 K Limit. *Nanoscale* **2015**, *7*, 10101−10110.
(75) Cheng, Z.; Liu, L. J.; Xu, S.; Lu, M.; Wang, X. W. Temperature Dependence of Electrical and Thermal Conduction in Single Silver Nanowire. *Sci. Rep.* **2015**, *5*, 10718.
(76) Deng, C. H.; Sun, Y. M.; Pan, L. J.; Wang, T. Y.; Xie, Y. S.; Liu, J.; Zhu, B. W.; Wang, X. W. Thermal Diffusivity of a Single Carbon Nanocoil: Uncovering the Correlation with Temperature and Domain Size. *ACS Nano* **2016**, *10*, 9710−9719.

DOI: 10.1021/acsnano.9b00031
ACS Nano 2019, 13, 5385−5396